

---

# REORIENTING OFF-PATH NUDGED ELASTIC BANDS (RONEB) VIA MINIMUM MODE FOLLOWING

---

A PREPRINT

 **Rohit Goswami\***

Institute IMX and Lab-COSMO

École polytechnique fédérale de Lausanne (EPFL)

Station 12, CH-1015 Lausanne, Switzerland

and

Science Institute & Faculty of Physical Sciences  
University of Iceland, 107 Reykjavík, Iceland

[rgoswami@ieee.org](mailto:rgoswami@ieee.org)

 **Miha Gunde**

Institute Ruder Boskovic

Bijenicka 54, 10000 Zagreb

Croatia

and

Science Institute & Faculty of Physical Sciences  
University of Iceland  
107 Reykjavík, Iceland

[mgunde@irb.hr](mailto:mgunde@irb.hr)

 **Hannes Jónsson**

Science Institute & Faculty of Physical Sciences

University of Iceland

107 Reykjavík, Iceland

[hj@hi.is](mailto:hj@hi.is)

January 21, 2026

## ABSTRACT

Accurate determination of transition states remains central to understanding reaction kinetics. Double-ended methods like the Nudged Elastic Band (NEB) ensure relevant transition states and paths, but incur high computational costs and suffer stagnation on flat or rough potential energy surfaces. Conversely, single-ended eigenmode-following techniques offer efficiency but cannot often be constrained between specific states. Here, we present the Reorienting Off-path Nudged Elastic Bands (RONEB), an adaptive hybrid algorithm that integrates the double ended nature of the NEB with the acceleration of single ended Min-Mode Following methods. RONEB provides stability based on the history of the path optimization, relative force triggering, and an alignment-based back-off penalty to dynamically decouple the climbing image from the elastic band constraints. We benchmark the method against the standard Climbing Image NEB (CI-NEB) across the Baker-Chan transition state test set using the PET-MAD machine-learned potential and the OptBench Pt(111) heptamer island surface diffusion set. A Bayesian analysis of the performance data quantifies a median reduction in gradient calls of 46.3% [95% CrI: -54.7%, -36.9%] relative to the baseline, while surface diffusion tests reveal a 28% reduction across 59 metallic rearrangement mechanisms. These results establish RONEB as a highly effective tool for high-throughput automated chemical discovery.

**Keywords** Transition State Search, Nudged Elastic Band, Machine Learning Potentials, Bayesian Regression, Hybrid Optimization, Potential Energy Surface, Reaction Kinetics, High-Throughput Chemistry

## 1 Introduction

The formation energy for reactants transforming to products relies on an accurate determination of corresponding the energy barrier, leading to kinetic considerations. To find these barriers, we require the transition state, or the

---

\*Corresponding Author

dividing surface, a  $3N - 1$  dimensional hyperplane between the reactant basin from the product basin. In the harmonic approximation, we define the hyperplane as the surface passing through the first order saddle point which remains perpendicular to the unstable mode, or the eigenvector corresponding to the negative eigenvalue. This first order saddle point (FOSP), or the geometry corresponding to it, marks the point of highest energy along the minimum energy path, or MEP. The MEP passes through the FOSP, connecting the reactant and product minima and providing the most path of highest statistical weight in configuration space. For most computational chemists, the key benefit of transition state methods involves finding the chemical transformation pathway, since a first attempt at a rate estimate depends on the energy barrier and the ratio of the vibrational frequencies.

We may find saddle points by starting with two known states, the “Double-ended” methods, such as the Nudged Elastic Band or NEB [19], where a discrete chain of images or configurations connecting known reactants and products evolve to pass through the saddle point and relax to the MEP. While robust in defining the global path, these methods require computation of energy and forces for each configuration along the path, and if each point needs electronic structure levels of accuracy, the scaling quickly becomes unfeasible. Additionally, determining the parameters of an NEB requires finesse, with everything from the initial path to the optimizers modulating the convergence and efficiency. The NEB relies on images in the vicinity of the saddle point configuration, in turn controlled by the number of images along the path and the spring constant which holds images to the path. With incorrect spring constants, the NEB can be expensive and prone to stagnation on flat or rough potentials where projected spring forces struggle to resolve the saddle curvature. Conversely, “initial-point” methods, such as the Dimer method, require a single starting configuration and follow the lowest eigenmode of the Hessian directly to a saddle. Such minimum mode following searches don’t require the evaluation of many configurations for each traversal step. The unconstrained nature of the search, which frequently converges to irrelevant transition states unconnected to the reaction of interest often offsets the computational efficiency.

Herein, we describe the Reorienting off-path Nudged Elastic Bands (RONEB), a novel method integrating the stability of double-ended chain-of-states methods with the speed of single-ended min-mode following methods. Unlike previous approaches that posit “handing off” to TS state searches at a given threshold [1, 30], RONEB tracks the history of the optimization to dynamically trigger local refinement only when the indices of the NEB are stable. We show that by coupling this adaptive triggering with an alignment-based cool-down strategy, RONEB accelerates convergence, nearly halving the number of calls even on universal machine-learned potential energy surfaces while avoiding the instabilities common to naive hybrid schemes.

## 2 Methods

We introduce the dimer and the nudged elastic band in a self-contained manner as implemented in the EON<sup>2</sup> software suite [8] before covering the novel RONEB algorithm.

### 2.1 Minimum Mode Following: The Dimer Method

To locate first-order saddle points without the computationally prohibitive evaluation of the full Hessian matrix, we use minimum mode following algorithms [mousseauActivationRelaxationTechniqueART2012 28] which conceptually trace back to state exploration methods [4]. Here, we consider the Dimer method [15, 29], which guides the search along the eigenvector corresponding to the lowest curvature of the PES.

The “dimer” consists of two system replicas or images,  $\mathbf{R}_1$  and  $\mathbf{R}_2$ , separated by a small finite distance  $\Delta R$  from a central point  $\mathbf{R}$  along a normalized orientation vector  $\hat{\mathbf{N}}$

$$\mathbf{R}_{1,2} = \mathbf{R} \mp \frac{\Delta R}{2} \hat{\mathbf{N}}. \quad (1)$$

Optimization proceeds in two interleaved steps: rotation and translation. First, the dimer rotates to minimize the total energy, thereby aligning  $\hat{\mathbf{N}}$  with the lowest curvature mode. We estimate the curvature  $C$  along the dimer axis via finite difference of the forces acting on the endpoints

$$C(\hat{\mathbf{N}}) \approx \frac{(\mathbf{F}_2 - \mathbf{F}_1) \cdot \hat{\mathbf{N}}}{\Delta R}. \quad (2)$$

Once aligned, the central configuration  $\mathbf{R}$  translates according to a modified effective force  $\mathbf{F}_{\text{trans}}$ . This force inverts the component of the true force  $\mathbf{F}(\mathbf{R})$  along the minimum mode, effectively transforming the saddle point into a local minimum for an optimizer

$$\mathbf{F}_{\text{trans}}(\mathbf{R}) = \mathbf{F}(\mathbf{R}) - 2(\mathbf{F}(\mathbf{R}) \cdot \hat{\mathbf{N}})\hat{\mathbf{N}}. \quad (3)$$

<sup>2</sup>From <https://eondocs.org>

## 2.2 Nudged Elastic Band – NEB

For double-ended searches requiring the full MEP between known reactant and product states, we consider the Nudged Elastic Band method. The NEB approximates the reaction pathway as a chain of “images” connected by fictitious springs, so we have

$$\mathbf{F}_i^{\text{NEB}} = \mathbf{F}_i^{\perp} + \mathbf{F}_i^{\parallel, \text{spring}}. \quad (4)$$

The method maintains path continuity and spacing by projecting force components. We apply the true potential force only perpendicular to the path tangent

$$\mathbf{F}_i^{\perp} = \mathbf{F}_i^{\text{true}} - (\mathbf{F}_i^{\text{true}} \cdot \hat{\tau}_i) \hat{\tau}_i, \quad (5)$$

while spring forces act only parallel to it

$$\mathbf{F}_i^{\parallel, \text{spring}} = k(|\mathbf{R}_{i+1} - \mathbf{R}_i| - |\mathbf{R}_i - \mathbf{R}_{i-1}|) \hat{\tau}_i. \quad (6)$$

This “nudging” prevents the band from cutting corners or sliding down into minima.

To ensure numerical stability, we use the “improved tangent” estimate [16], which defines the tangent based on the energy of neighboring images to reduce the probability of kinks in the path:

$$\hat{\tau}_i = \begin{cases} \text{normalize}(\mathbf{R}_{i+1} - \mathbf{R}_i) & \text{if } V_{i+1} > V_i > V_{i-1} \\ \text{normalize}(\mathbf{R}_i - \mathbf{R}_{i-1}) & \text{if } V_{i-1} > V_i > V_{i+1} \\ \text{weighted average} & \text{otherwise} \end{cases} \quad (7)$$

At extrema, we define the tangent to be the weighted average of the vectors to neighboring images, giving preference to the vector on the higher energy side.

To determine only the saddle point instead of resolving the entire path, modifications to the involve the “climbing image” [17], where the highest energy image has the spring force removed, and the parallel component inverted, which forces the image, identified as the “climbing” image to move uphill along the path to the saddle point.

$$\mathbf{F}_{\text{climb}} = \mathbf{F}_{\text{climb}}^{\text{true}} - 2(\mathbf{F}_{\text{climb}}^{\text{true}} \cdot \hat{\tau}_{\text{climb}}) \hat{\tau}_{\text{climb}} \quad (8)$$

The accuracy of the saddle configuration depends on the tangent approximation, which in turn derives from the neighboring images of the climbing image. To increase the resolution of images around the saddle without increasing the number of images, we may adjust the springs, either through geometric considerations [1] or kinetic considerations [24].

The energy-weighted spring method [1] used here, dynamically stiffens the spring constant in high-energy regions, concentrating the chain to enforce higher image densities where the PES curvature should be resolved most accurately.

The quality of the initial path influences convergence speed and stability. Linear interpolations often produce unphysical atomic overlaps, particularly for complex or dense systems. To mitigate this without having to construct new paths for every system, improved initial paths in Cartesian Coordinates can be constructed, by using the Sequential Image Dependent Pair Potential (S-IDPP) method [32, 33].

S-IDPP constructs the path by sequentially growing images from the reactant and product endpoints. It optimizes these intermediate images on a simplified auxiliary surface defined by interpolating the pairwise distances of bonded atoms in the endpoints. This procedure attempts to eliminate high-energy steric clashes before engaging computationally expensive DFT or MLIP forces.

## 2.3 Reorienting off-path Nudged Elastic Bands (RONEB)

The standard Climbing Image Nudged Elastic Band, or CINEB depends on the efficiency of the underlying optimizer. Near transition states, or on flat or noisy sections of the PES, the projected force components can oscillate or become ill-defined. To address this, we introduce the RONEB algorithm, a hybrid approach that intersperses standard CINEB optimization steps with targeted MMF refinement using the Dimer method as implemented in EON<sup>3</sup>[18, 29]. This method works as a two-stage refinement strategy within each NEB iteration once the path relaxes [8]. The core concept involves using the robust path-finding capability of NEB to bring the climbing image close to the saddle point, and then

<sup>3</sup><https://eondocs.org>

switch to a more aggressive and efficient local saddle search algorithm for a few steps to rapidly refine the climbing image’s position.

In practice, a fixed number of steps like the CINEB-MMF [8] and a single threshold for activation don’t transfer across benchmark systems and energy surfaces. Workflow methods [30], or manual calculations [1] to run initial point methods after roughly converging the NEB algorithm to a given threshold may not find the appropriate saddle connecting the reactant and product basins even with an accelerated methods [10, 11].

RONEB dynamically switches between the NEB and dimer during a single calculation, thus taking inspiration from the active learning set of acceleration methods [10, 11, 21, 22, 31]. We develop the algorithm iteratively by solving stability and efficiency challenges inherent to such hybridization of methods.

### 2.3.1 Dynamic Control via Mode Alignment

A primary challenge for hybrid methods involves determining the duration of the refinement phase. RONEB utilizes the alignment between the minimum mode of the Hessian eigenmode  $\hat{v}_{min}$  and the global path tangent  $\hat{\tau}$ . By initializing the Dimer along  $\hat{\tau}$ , we ensure the local search begins in a relevant subspace, preventing initialization based failures [10]. The alignment between the two,

$$\alpha = |\hat{v}_{min} \cdot \hat{\tau}| \quad (9)$$

serves as a convergence criteria. The MMF continues while the orientation remains close to the tangent estimate. If the angle becomes orthogonal to the path, the search aborts immediately, but we use the history of the optimizer to move the climbing image along the dimer trajectory to the positions with the most negative eigenvector. This dynamic termination based on the path estimate replaces arbitrary step counts.

### 2.3.2 Relative Baselines and Transferability

An interesting caveat comes from high throughput considerations, given that we generate initial paths using the S-IDPP which may involve high energy initial paths, defining the “handover point” or the force threshold at which the algorithm switches from the NEB to MMF becomes problematic. Absolute force thresholds say, 0.5 eV/Å don’t make sense across a diverse dataset since a value appropriate for a stiff covalent bond breakage may correspond to an effectively converged state for a soft supramolecular rearrangement.

To mitigate this, we establish a relative baseline. At the start of the calculation, we record the baseline force ( $F_0$ ) of the initial path. We then express the triggering threshold  $T_{mmf}$  as a fraction of this baseline:

$$T_{mmf} = \lambda_{trigger} F_0. \quad (10)$$

This ensures the algorithm engages only after the NEB has relaxed the high-energy conflicts from the initial guess, regardless of the absolute energy scale of the system.

### 2.3.3 Robustness: Stability Latches and Restoration

In practice, activating MMF based solely on force thresholds can lead to instability for rough potentials or where the climbing image index oscillates. RONEB implements a stability latch, engaging local refinement only if the climbing image index remains constant for iterations.

The internal state of the optimizer resets if the motion of the image exceeds the maximum move of each image times the total number of intermediate images. Furthermore, as noted earlier, we implement a “best-state” restoration mechanism. If the MMF calculation terminates, either due to failure from the alignment check or by entering a region of positive curvature, we don’t accept the final coordinates for the climbing image. Instead, we move the climbing image to the configuration with the most negative curvature found during the search. This allows RONEB to recover partial progress from a failed MMF searches before returning control to the NEB.

### 2.3.4 Adaptive Back-off

Finally, to prevent the algorithm from repeatedly triggering MMF in regions with poor alignment to the tangent, we use an adaptive back-off strategy. If a local refinement attempt fails or degrades the alignment, we penalize the triggering threshold  $T_{mmf}$ :

$$P(\alpha) = B + (1 - B)\alpha^S \quad (11)$$

$$T_{mmf}^{next} = F_{CI} \times P(\alpha) \quad (12)$$

This dynamically pushes the trigger point to a lower force, compelling the global NEB to perform significant relaxation and realignment before performing more local searches.

### 2.3.5 Complete Algorithm

Taken together, the RONEB algorithm proceeds as noted in Algorithm 1.

---

**Algorithm 1** Reorienting off-path Nudged Elastic Bands (RONEB)

---

```

1: Input: Initial Path  $\mathcal{P} = \{\mathbf{R}_0, \dots, \mathbf{R}_{P+1}\}$ , Baseline Force  $F_0$ 
2: Parameters: Trigger  $\lambda = 0.45$ , Stability  $\kappa = 5$ , Penalty Base  $B = 0.2$ , Penalty strength  $S = 1.0$ 
3:  $T_{mmf} \leftarrow \lambda F_0$ 
4:  $L_{stable} \leftarrow 0$ 
5: while not converged do
6:   Find highest energy image,  $\mathbf{R}_{climb}$  (index  $k$ )
7:   Calculate tangents  $\hat{\tau}_i$  and NEB forces  $\mathbf{F}^{NEB}$ 
8:   Calculate climbing image force  $F_{CI} = \|\mathbf{F}_{climb}\|$ 
9:   if  $k == k_{prev}$  then
10:     $L_{stable} \leftarrow L_{stable} + 1$ 
11:   else
12:     $L_{stable} \leftarrow 0$ 
13:   end if
14:   if  $L_{stable} \geq \kappa$  and ( $F_{CI} < T_{mmf}$  or  $F_{CI} < T_{abs}$ ) then ▷ Switch to local MMF refinement
15:     Initialize Dimer at  $\mathbf{R}_k$  with orientation  $\hat{\tau}_k$ 
16:     Run MMF Optimization:
17:       Optimize  $\mathbf{R}_k$  along minimal mode  $\hat{\mathbf{v}}_{min}$ 
18:       Check: If curvature  $> 0$  or alignment  $\alpha < \alpha_{tol}$ , Abort
19:       Recovery: If aborted, restore position of best negative curvature
20:       Update Alignment  $\alpha = |\hat{\mathbf{v}}_{min} \cdot \hat{\tau}_k|$ 
21:       if MMF Successful and  $F_{new} < F_{CI}$  then
22:         Relax threshold:  $T_{mmf} \leftarrow F_{new} \cdot (0.5 + 0.4 \frac{F_{new}}{F_{CI}})$ 
23:       else
24:         Apply Penalty:  $T_{mmf} \leftarrow F_{CI}(B + (1 - B)\alpha^S)$ 
25:       end if
26:       Update forces for  $\mathcal{P}$ 
27:       if  $\|\mathbf{R}_k^{new} - \mathbf{R}_k^{old}\| > \Delta_{tol}$  then
28:         Reset Global Optimizer History
29:       end if
30:       Take a global optimization step on  $\mathcal{P}$ 
31:     else
32:       Take a global optimization step on  $\mathcal{P}$  ▷ Perform standard NEB optimization step
33:     end if
34:    $k_{prev} \leftarrow k$ 
35: end while

```

---

1. Configuration The RONEB implementation exposes tunable parameters that control the aggressiveness of the local search. Table 1 lists these parameters alongside their corresponding configuration keys and default values used in this work.

Table 1: **RONEB Configuration Parameters.**

Parameter Description	Symbol	Config Key	Default Value
Relative Trigger Factor	$\lambda_{rel}$	ci_mmf_after_rel	0.5
Absolute Trigger Floor	$\lambda_{abs}$	ci_mmf_after	0.1 eV/Å
Max MMF Steps	$N_{mmf}$	ci_mmf_nsteps	1000
Alignment Tolerance	$\alpha_{tol}$	ci_mmf_angle	0.9
Penalty Strength	$S$	ci_mmf_penalty_strength	1.5
Penalty Base	$B$	ci_mmf_penalty_base	0.4
Stability Count	$\kappa$	ci_mmf_ci_stability_count	5

While the configuration allows for granular control, the “Alignment Tolerance,”  $\alpha_{tol}$  and the “Relative Trigger Factor,”  $\lambda_{rel}$  emerge as the primary determinants of algorithmic efficiency. The remaining parameters fulfill specialized roles, particularly within automated high-throughput workflows.

For instance, the “Absolute Trigger Floor,”  $\lambda_{abs}$  often functions as the main activation criterion for single-reaction studies with known energy scales, whereas the relative factor ensures transferability across diverse barrier heights in blind searches. Similarly, the step limit  $N_{mmf}$  governs the synchronization frequency between the local dimer search and the global path constraints. Finally, the penalty parameters,  $S$  and  $B$  enable an adaptive back-off mechanism to handle topological mismatch. We leave a detailed analysis of these stability features and the specific influence of the primary control knobs for Section 4.

## 2.4 Computational Details

All calculations use the EON software package<sup>4</sup>. The Metatomic interface [3] to the PET-MAD v1.1.0 machine learning interatomic potential [25, 26] provides energy and forces. This non-equivariant point-edge transformer model trained on the diverse MAD dataset, encompassing bulk crystals, surfaces, and molecular fragments at the PBEsol functional level. A Snakemake [27] workflow orchestrated concurrent runs on a single machine with an AMD Ryzen Threadripper PRO 5945WX (24 core, 48 threads) and an NVIDIA T400 GPU with 4GB VRAM. For efficient concurrency on the singular GPU, we use the NVIDIA multi-processing service. As per established best practices [7, 20] we use the limited-memory Broyden-Fletcher-Goldfarb-Shanno [23] for translation and the conjugate gradient optimizer [5] for rotations.

We assessed the performance of the RONEB algorithm against the standard CINEB method across the 25 reactions of the Baker transition state test suite. The Baker and Chan set of 25 reactions [2] covers broad chemical archetypes, including systems undergoing dissociations ( $\text{H}_2\text{CO}$ ), insertions (silene), ring-opening (cyclopropyl), and rotational transitions (acrolein). Since these systems exhibit diverse PES features, ranging from stiff covalent bonds to weak intermolecular forces, they provide rigorous test for the adaptability and robustness of RONEB compared to the standard CINEB protocol.

Both methods utilized identical initialization parameters (S-IDPP [32], 8 intermediate images) and convergence criteria (0.05eV/Å). Baseline CINEB and the RONEB protocols utilized identical optimization backends and convergence criteria. The specific hyperparameters governing the hybrid RONEB triggers are detailed in Table 2.

Table 2: **Optimization hyperparameters.** Shared parameters apply to both methods. RONEB-specific parameters govern the activation and stability of the local dimer search.

Category	Parameter	Symbol	Value
Shared	Potential	$V(\mathbf{R})$	PET-MAD v1.1
	Optimizer	-	LBFGS
	Convergence Force	$F_{tol}$	0.05 eV/Å
	Images	$N_{img}$	8
	Spring Constant	$k_{sp}$	0.97 – 9.72 eV/Å <sup>2</sup> (Energy Weighted)
	CI Activation (Relative)	$\lambda_{CI}$	0.8
	S-IDPP Growth Factor	$\alpha_{idpp}$	0.33
RONEB	MMF Relative Trigger	$\lambda_{mmf}$	0.5
	Alignment Tolerance	$\cos \theta_{tol}$	0.9
	Penalty Strength	$S$	1.5
	Penalty Base	$B$	0.4
	Dimer Rot. Convergence	$\phi_{tol}$	10.0°

Both methods converge for all systems, and the RONEB strictly improves performance in every case, so we use a hierarchical Bayesian negative binomial regression with varying slopes modeled via B-splines with an intercept for each system for quantifying the performance as a function of the distance of the initial path saddle estimate to the final configuration [7, 8, 10]. Distances [9] used involve permutation corrections through the iterative rotations and assignments algorithm [14]. The SI contains complete details.

Many methods end up hyperfocused on synthetic benchmarks without considering the wider applicable range of the underlying methods. The NEB finds use not only for gas phase molecular systems, but primarily for extended systems. We use the OptBench [6] Pt(111) heptamer island benchmark, which focuses on metallic surface diffusion. This dataset contains 59 low-energy mechanisms for the rearrangement of a platinum heptamer on a Pt(111) slab. To strictly adhere

<sup>4</sup><https://eondocs.org>

to the benchmark definition, these calculations employed an analytic Morse potential (`morse.pt`) rather than the MLIP. The setup involved 5 intermediate images initialized via linear interpolation, without energy weighted springs and a fixed spring constant of 5. We enforced a tighter convergence criterion of 0.001 eV/Å for the force norm. Frozen atoms in the bottom slab eliminated rotational and translational degrees of freedom, rendering the removal of these modes unnecessary. The RONEB and CINEB parameters are otherwise identical to those in Table 2.

### 3 Results

The OptBench Pt(111) heptamer benchmark probes efficiency in the regime of solid-state surface diffusion. Table 3 summarizes the performance statistics. Despite the use of a simple linear initialization and a tighter convergence criterion (0.001 eV/Å), RONEB demonstrates superior efficiency. The hybrid protocol reduced the mean computational cost by approximately 28%, dropping from 397 force calls with CINEB to 286 with RONEB. Wall-clock time reflected this gain, with the mean optimization time decreasing from 2.44 seconds to 1.11 seconds. This speedup occurred without compromising accuracy. The average RMSD between the final saddle point configurations stood at  $6.8 \times 10^{-5}$  Å, with energetic differences remaining effectively zero. This confirms that RONEB reliably locates the same transition states as the baseline CINEB, even when applied to metallic surface diffusion processes where multiple competing mechanisms lie in close proximity.

Table 3: Statistical summary of the Pt(111) Heptamer Island benchmark. Values represent gradient evaluations across the 59 diffusion mechanisms.

Metric	CINEB	RONEB	Reduction
Mean	397	286	28%
Median	372	298	20%
Min	172	92	47%
Max	1172	860	27%

While the OptBench Pt(111) heptamer benchmark probes efficiency for solid-state surface diffusion, the Baker-Chan set effectively probes molecular reactions in the gas phase. Table 4 summarizes the computational cost for each system in the Baker-Chan benchmark. RONEB demonstrates a consistent advantage, yielding a mean reduction in force evaluations of approximately 44% across the dataset.

Figure 1 visualizes the system-specific efficiency gains. The breakdown demonstrates that the performance differential varies across the test set. For straightforward rearrangements (e.g., 07, 19), both methods perform comparably. For systems exhibiting larger structural reorganizations or flatter potential energy landscapes (e.g., 06, 18, 24), the gap widens. The “dumbbell” spans in Figure 1 illustrate these reductions, indicating that RONEB prevents the cost blowouts associated sections of configuration space with near zero forces.

Figure 2 illustrates the dependence of computational effort on the quality of the initial guess. Both algorithms exhibit a log-linear increase in the energy and gradient evaluation calls as the initial structural displacement grows, reflecting the fundamental nature of chain-of-states methods: distal starting points require more iterations to drag the elastic band toward the saddle. RONEB establishes a consistent efficiency offset, operating strictly below the cost trajectory of CINEB across the sampled domain.

In the near-harmonic regime around the transition state, the RMSD between the initial estimate and final configurations remains low; so the credible intervals for the methods overlap, indicating parity.

Since the initial path lies sufficiently close, the NEB relaxes rapidly, often converging before the MMF trigger condition can provide significant acceleration. As the displacement increases, the robust advantage of the hybrid protocol becomes clear. The MMF phase activates at the climbing image, effectively decoupling the saddle search from the stiff elastic band. This lowers the pre-factor of the cost scaling, ensuring that RONEB maintains a lower computational burden even as the search space expands.

To further contextualize these performance gains, Figure 3 contrasts structural difficulty with energetic difficulty. Panel C suggests a lack of correlation between the reaction barrier height and the computational cost. While one might expect higher barriers to require more energy and gradient evaluations, the data indicates that the distance of the saddle configuration from the reactant shown in Figure 2 serves as the primary driver of optimization effort. Panel B confirms that this efficiency doesn’t come at the cost of accuracy and the RONEB identifies transition states with a structural deviation of around 0.01 Å from the CINEB reference in all almost every case. This suggests that the “stiffness” of the optimization problem derives more from the “memory” of the initial path than the height of the hill, reinforcing the value of RONEB decoupling from the neighboring images.

Table 4: Comparison of total force evaluations for CINEB and RONEB on the Baker test set. *Diff* indicates the reduction in evaluations achieved by RONEB.

ID	Reaction	CINEB	RONEB	Diff	RMSD
01	$\text{HCN} \longrightarrow \text{HNC}$	202	177	25	$3.35 \times 10^{-4}$
02	$\text{HCCH} \longrightarrow \text{CCH}_2$	546	300	246	$1.34 \times 10^{-3}$
03	$\text{H}_2\text{CO} \longrightarrow \text{H}_2 + \text{CO}$	882	374	508	$7.33 \times 10^{-4}$
04	$\text{CH}_3\text{O} \longrightarrow \text{CH}_2\text{OH}$	330	228	102	$1.41 \times 10^{-3}$
05	cyclopropyl ring opening	202	115	87	$5.83 \times 10^{-3}$
06	bicyclo[1.1.0]butane $\rightarrow$ <i>trans</i> -butadiene	1066	358	708	$1.35 \times 10^{-2}$
07	formyloxyethyl 1,2-migration	242	217	25	$1.11 \times 10^{-2}$
08	parent Diels-Alder cycloaddition	722	353	369	$1.33 \times 10^{-2}$
09	s-tetrazine $\longrightarrow 2 \text{ HCN} + \text{N}_2$	594	198	396	$1.34 \times 10^{-2}$
10	<i>trans</i> -butadiene $\rightarrow$ <i>cis</i> -butadiene	242	179	63	$2.59 \times 10^{-2}$
11	$\text{CH}_3\text{CH}_3 \longrightarrow \text{CH}_2\text{CH}_2 + \text{H}_2$	450	224	226	$1.85 \times 10^{-2}$
12	$\text{CH}_3\text{CH}_2\text{F} \longrightarrow \text{CH}_2\text{CH}_2 + \text{HF}$	450	154	296	$3.63 \times 10^{-3}$
13	acetaldehyde keto-enol tautomerism	394	233	161	$3.44 \times 10^{-2}$
14	$\text{HOCl} \longrightarrow \text{HCl} + \text{CO}$	298	135	163	$1.89 \times 10^{-3}$
15	$\text{H}_2\text{O} + \text{PO}_3^- \longrightarrow \text{H}_2\text{PO}_4^-$	1226	887	339	$3.26 \times 10^{-2}$
16	$\text{CH}_2\text{CHCH}_2\text{CH}_2\text{CHO}$ Claisen rearrangement	2026	1975	51	$7.01 \times 10^{-2}$
17	$\text{SiH}_2 + \text{CH}_3\text{CH}_3 \longrightarrow \text{SiH}_3\text{CH}_2\text{CH}_3$	482	356	126	$2.76 \times 10^{-2}$
18	$\text{HNCCS} \longrightarrow \text{HNC} + \text{CS}$	3954	1883	2071	$3.18 \times 10^{-1}$
19	$\text{HCONH}_3^+ \longrightarrow \text{NH}_4^+ + \text{CO}$	482	477	5	$2.17 \times 10^{-2}$
20	acrolein rotational TS	394	166	228	$1.56 \times 10^{-2}$
21	$\text{HCONHOH} \longrightarrow \text{HCOHNHO}$	322	201	121	$1.45 \times 10^{-2}$
22	$\text{HNC} + \text{H}_2 \longrightarrow \text{H}_2\text{CNH}$	778	378	400	$3.42 \times 10^{-3}$
23	$\text{H}_2\text{CNH} \longrightarrow \text{HCNH}_2$	490	137	353	$7.20 \times 10^{-3}$
24	$\text{HCNH}_2 \longrightarrow \text{HCN} + \text{H}_2$	2202	996	1206	$4.93 \times 10^{-3}$
<b>Mean</b>		790.7	445.9	344.8	$2.75 \times 10^{-2}$
<b>Median</b>		482.0	230.5	227.0	$1.33 \times 10^{-2}$

The highest RMSD between the saddle of the CINEB and the RONEB ( $0.32 \text{ \AA}$ ) corresponds to the HNCCS aggregation reaction in System 18, with the RONEB delivering a massive reduction in cost of 1883 vs. 3954 force calls. While this structural deviation appears to exceed the typical tolerance for identical convergence, the energetic profiles in Figure 4 reveals that both methods located the same valid transition state on a flat potential energy ridge.

## 4 Discussion

The relationship between initial guess quality and computational cost demonstrates the robustness advantage for the local dimer acceleration. As shown in Figure 2, the scaling profiles diverge as the initial RMSD increases. For good estimates of the initial saddle configuration, ( $\text{RMSD} < 0.3 \text{ \AA}$ ), the performance remains parity-bound. In the regime of poor initialization ( $\text{RMSD} > 0.6 \text{ \AA}$ ), CINEB exhibits a steep efficiency penalty, whereas RONEB maintains a flatter cost trajectory. This confirms that the decoupling of the reaction path allows the dimer method to recover efficiently from poor starting geometries without the path-elasticity artifacts that hamper the NEB. Similar effects exist for other acceleration schemes [12], in all cases, we expect systems which take more iterations to have better gains from such techniques.

Starting the MMF early can lead to a separate, higher energy saddle when seeded with a poor initial path. Consider the keto-enol tautomerism of vinyl alcohol, `14_vinyl_alcohol`. An interesting aside involves the initial conditions for this system. The IRA [14] algorithm in this instance, when applied to the endpoints, re-orders the H atom to drive a 1,2-hydrogen shift along the C-C bond. Although energetically unfavorable, this permutation yields a lower Euclidean distance than the chemically correct 1,3-arch. An initial path generated from the permuted endpoints forces the hydrogen atom through the dense electron density of the C-C bond, creating a massive artificial steric barrier. Purely geometric alignment metrics can't handle such situations, though for many cases including this one, masking the hydrogen atoms and aligning the heavier elements before using the Constrained Shortest Distance Assignments or

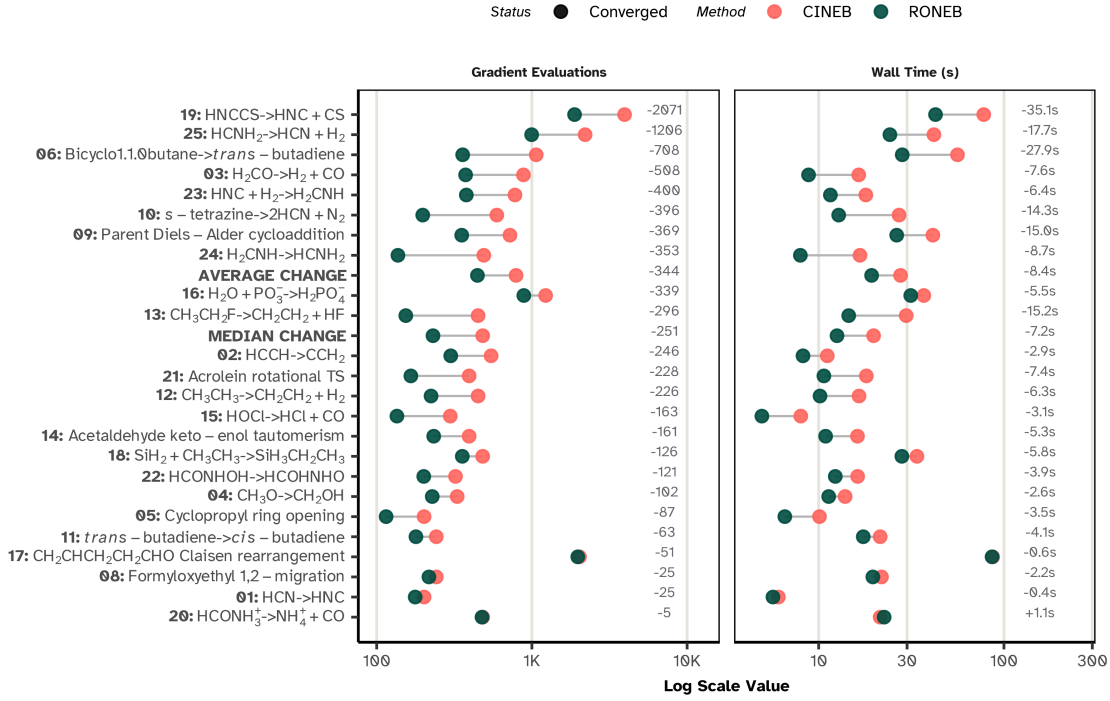


Figure 1: **Comparative computational cost for the test set of transition configurations** [2]. The “dumbbell” spans illustrate the reduction in gradient evaluations (left) and wall-clock time (right) achieved by RONEB (teal) relative to CINEB (coral).

CShDA or point group symmetry measures [13] can fix ordering concerns. To keep our focus on the RONEB, we report results based on the coordinates from the initial structures without alignment, as the endpoint alignment forms part of the initial path considerations not covered here, but actively worked on for a follow-up.

The efficiency of the hybrid RONEB scheme relies on three coupled parameters that govern the “handover” from the collective band optimization to the local saddle search. We interpret these physically as follows:

- **The Patience Factor** This relative force threshold, configured by `ci_mmff_after_rel`, determines the degree of path relaxation required before a MMF calculation begins. A high value (e.g.,  $0.8 \times F_{init}$ ) implies high “trust” in the initial path topology, attempting to snap to the saddle early to minimize collective gradient calls. A low value (e.g.,  $0.2 \times F_{init}$ ) enforces “patience,” effectively delaying the handover until the NEB has resolved the major features of the reaction valley and the climbing image is strictly positioned within the quadratic basin of the transition state.
- **The Topological Filter** This alignment criterion, controlled by `ci_mmff_angle` acts as a safety gate for the local mode. By requiring the dimer mode to align with the NEB tangent (e.g.,  $\alpha_{tol} > 0.9$ ), we ensure the MMF refines the specific barrier identified by the path. Loosening this tolerance allows the dimer to explore orthogonal directions, which can facilitate the discovery of lower-energy saddles but risks diverting the algorithm into chemically irrelevant rearrangement channels.
- **The Penalty Strength** The two parameters,  $S$  and  $B$  governs the algorithm’s resilience to mode mismatch. If the local dimer mode fails the topological filter or fails to lower the force, we dynamically suppress the trigger threshold ( $f_{new} \approx f_{old} \times \alpha^S$ ). A high penalty strength ( $S = 1.5$ ) enforces a “fail-fast” logic: if the MMF aborts we force the NEB to relax further to correct the tangent estimate before attempting to retry.

To provide a better intuition for these parameters, consider three runs for the system with the least improvement, the  $HCONH_3^+$  fragmentation, `20_hconh3_cation`. The interpolation provides a rather poor estimate of the minimum energy path, sampling configurations over 2eV relative to the reactant. For clarity, let us call these RONEB protocols—“Loose,” and “Strict,” where the settings used for the broader benchmark against the standard CINEB baseline we term as the “Reported” protocol. Table 5 details these configurations.

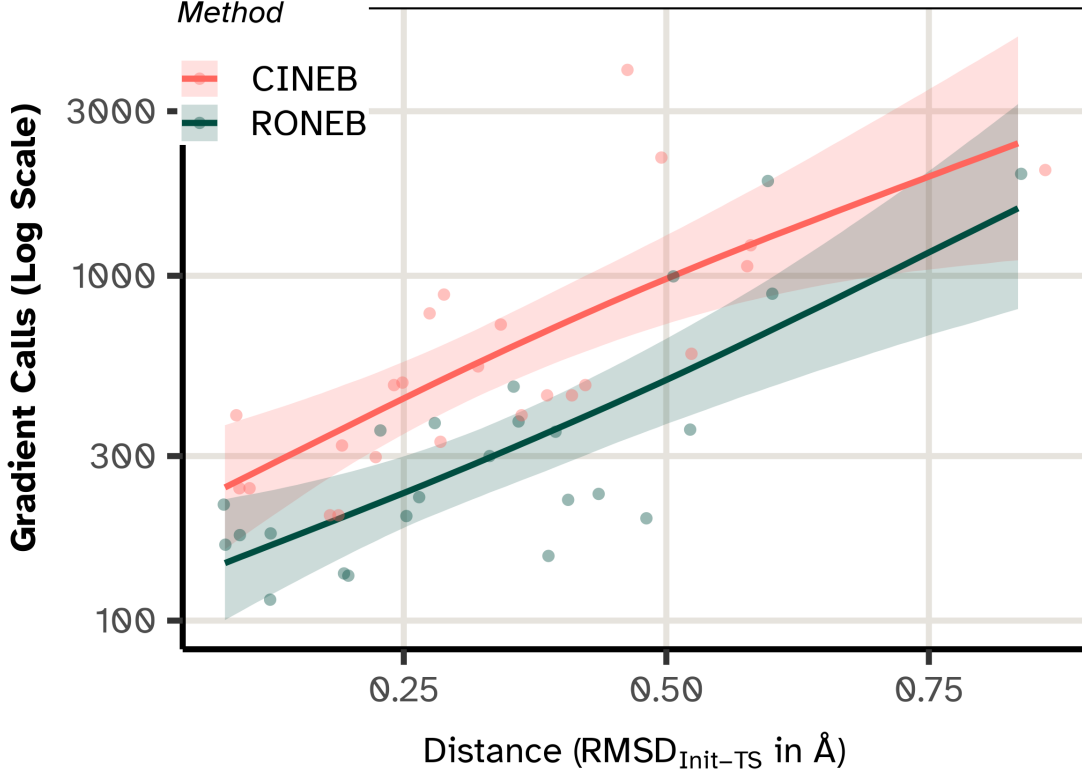


Figure 2: **Algorithmic robustness profile modeled via Bayesian negative binomial regression.** The plot tracks the predicted computational cost (gradient calls, log scale) as a function of the initial structural displacement from the final transition state. Shaded regions indicate 95% credible intervals. Both methods show a log-linear rise in cost with distance, but RONEB (teal) maintains a consistent efficiency advantage over CINEB (coral), demonstrating that the local MMF acceleration effectively lowers the computational overhead across the search space.

Table 5: Comparison of RONEB protocols applied to System 20. The “Reported” column corresponds to the global settings used in Table 2.

Parameter Description	Symbol	Loose	Reported Protocol	Strict
Relative Trigger Threshold	$f_{trigger}/F_0$	0.8	0.5	0.2
Tangent Alignment Tolerance	$\alpha_{tol}$	0.4	0.9	0.9
Penalty Strength	$S$	1.5	1.5	1.0
<b>Total Force Calls (Sys 20)</b>	$N_{calls}$	<b>695</b>	<b>477</b>	<b>385</b>

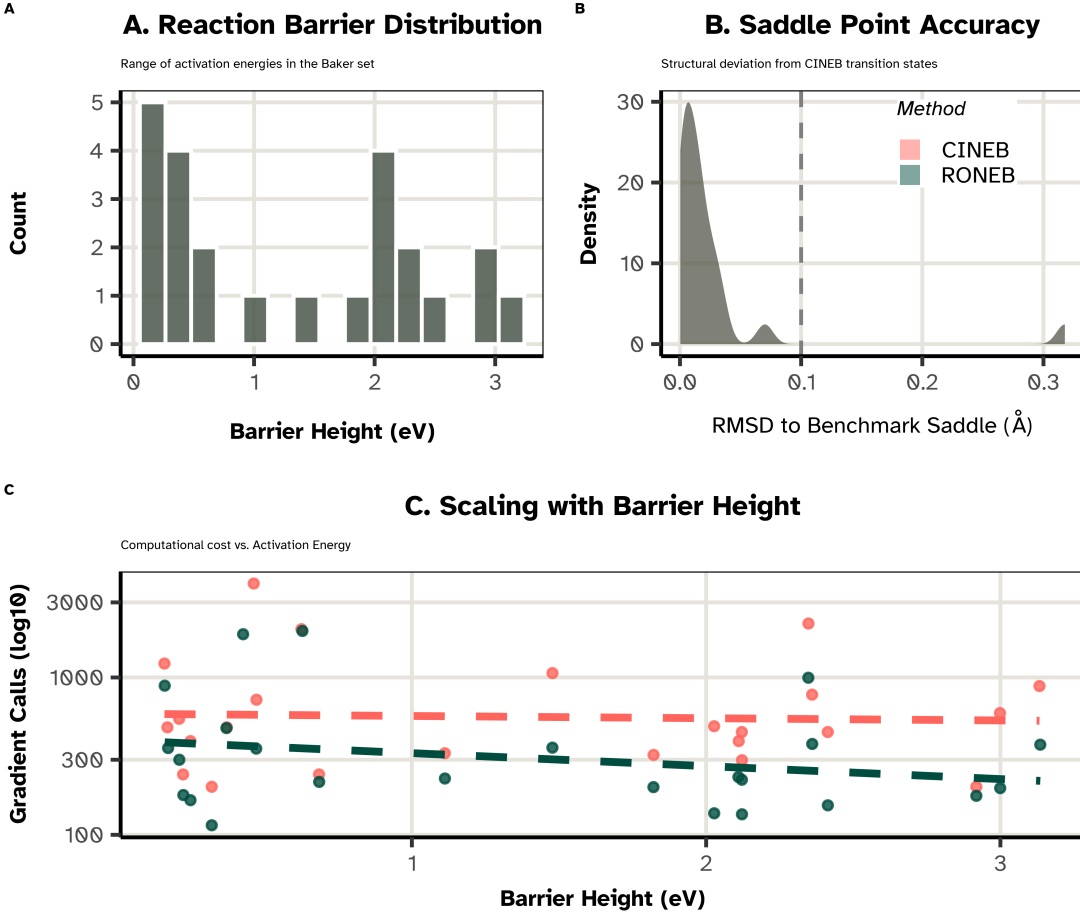


Figure 3: **Dataset Characterization and Drivers of Cost.** (A) Distribution of barrier heights in the test set. (B) Accuracy of RONEB compared to CINEB saddle points; the density peaks below 0.1 Å, confirming correct convergence. (C) Scatter plot of Computational Cost vs. Barrier Height. The lack of a strong trend contrasts with the clear scaling seen in Figure 2, indicating that initial structural guess quality drives cost more than the energetics of the reaction.

The “Loose” protocol triggers the local search prematurely at iteration 11 with  $F \approx 1.5 \text{ eV/Å}$ . At this stage, the elastic band remains high in energy, meaning the minimum mode at the climbing image can’t align with the correct orientation. The loose alignment filter of  $\alpha_{tol} > 0.4$  defined by Eq. 9 permits the dimer to lock onto this incorrect mode.

The logs and path traces in Figure 5 underscore this failure, wherein the dimer minimizes in a spurious direction, eventually failing to lower the projected force below the NEB baseline. This failure triggers the penalty mechanism of Eq. 11 with  $S = 1.5$ . This leads to the threshold force reducing, and the NEB path continuing. Because the algorithm accepts poor alignment, this cycle repeats at iterations 18 and 53, corresponding to wrinkles in the path. The accumulated overhead results in 695 force calls, exceeding the cost of the CINEB baseline of 482 calls.

In contrast, the “Strict” protocol enforces patience via a lower trigger of  $f_{trigger} = 0.2$  and a rigorous topological filter of  $\alpha_{tol} > 0.9$ . This bypasses the unstable early regime, waiting until iteration 24 with  $F \approx 0.46 \text{ eV/Å}$  to engage the MMF. By this point, the NEB has resolved the major features of the reaction valley. Crucially, the strict alignment check ensures the dimer only operates when the minimum mode and the path tangent agree. This protocol converged the system in 385 force calls, fully recovering the efficiency lost by the aggressive approach and outperforming the baseline by nearly a hundred calculations.

Despite this, we note that with reasonable initial paths, a more aggressive setting can vastly improve the efficiency of the RONEB and that applying the conservative settings globally reduces the acceleration for systems near convergence under initial conditions. Every one of the systems studied can improve performance by pre-processing parameters with a quick configuration fine-tuning run.

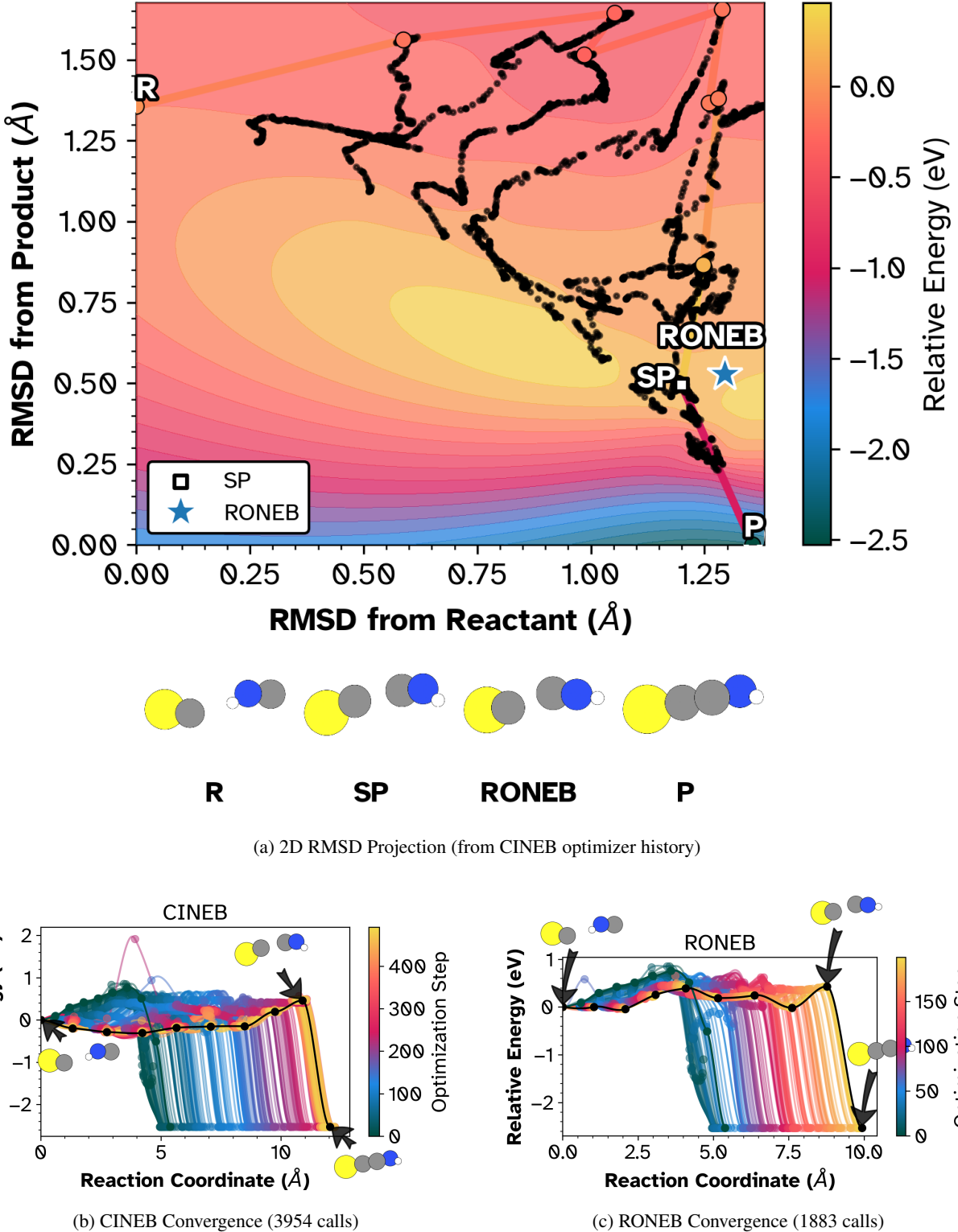


**Figure 4: Saddle Point Equivalence on the Flat HNCCS Landscape.** (A) A 2D projection of the potential energy surface. We utilize the denser CINEB trajectory points to generate the background contour, visualizing the extended ridge connecting the reactant and product basins [9]. The white square denotes the CINEB saddle, while the blue star indicates the RONEB result. (B) The baseline CINEB struggles to resolve regions of vanishing gradients, requiring nearly 4000 evaluations. (C) RONEB snaps to the saddle region early, terminating on the same energy isocontour with reduced computational effort.

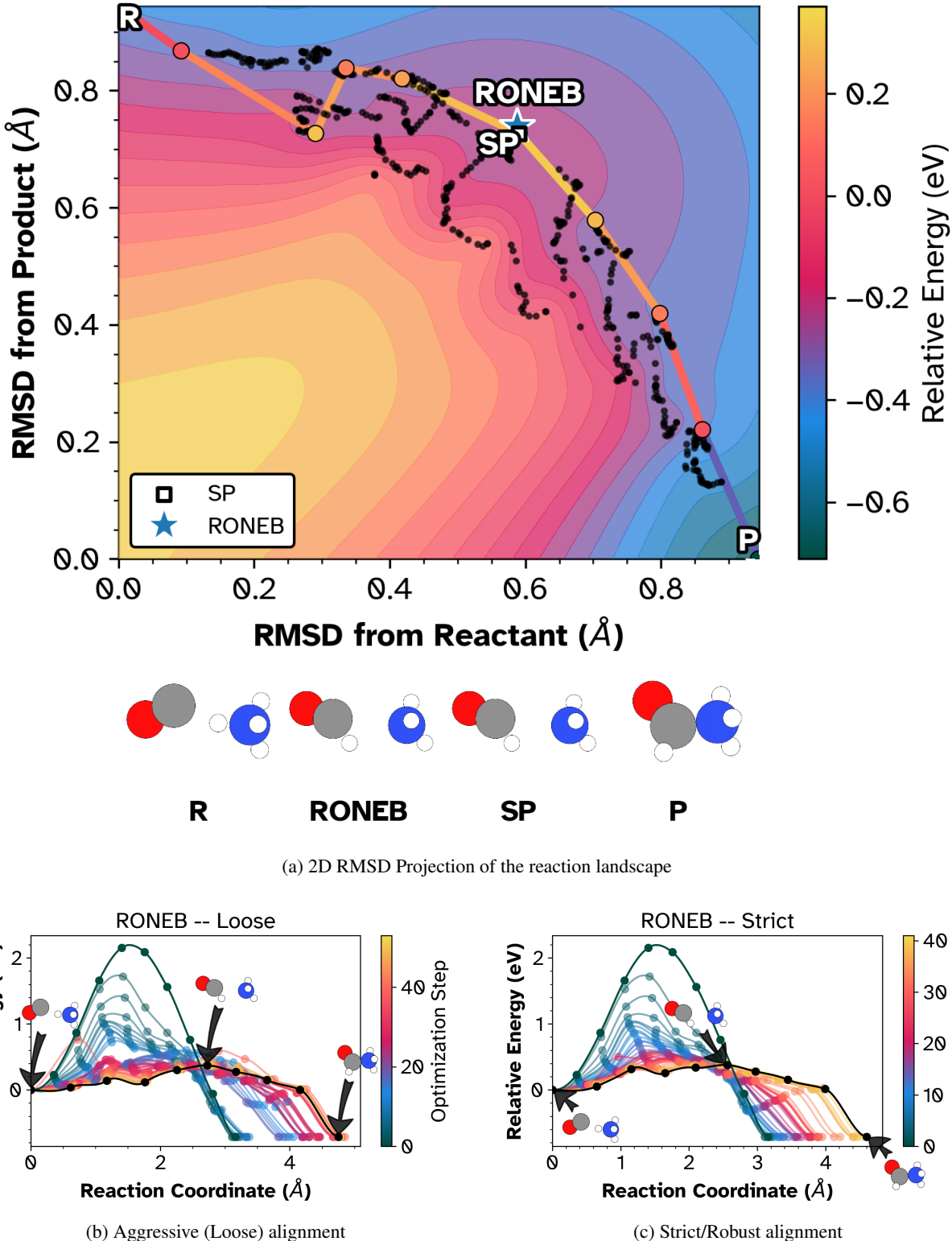


Figure 5: **Ablation study for  $\text{HCONH}_3^+$  fragmentation.** (A) A 2D projection of the potential energy surface illustrates the path evolution [9], confirming the numerical equivalence of the converged saddle points. (B-C) Convergence histories for the RONEB protocols. The aggressive configuration (B) initiates premature convergence, resulting in path oscillations. Conversely, the strict protocol (C) stabilizes the search by enforcing rigorous alignment tolerances.

The parameters reported in the previous section, using  $f_{trigger} = 0.5$  and  $\alpha_{tol} = 0.9$ ) occupy an effective middle ground. By delaying the trigger until the path forces drop by 50%, it avoids the initial instability of early MMF runs. By enforcing the strict 0.9 alignment tolerance, we keep the fail-fast safety mechanism, preventing the dimer from exploring far from the NEB path. This configuration converged System 20 in 477 force calls, delivering an enhancement to the baseline of 482 calls, while retaining the same saddle configuration. We selected these settings as the general-purpose recommendation for blind transition state searches, with the understanding that the method, like all NEB accelerations, requires some knowledge of the nature of the reaction considered.

## 5 Conclusions

We presented the RONEB algorithm, an adaptive hybrid optimization strategy that integrates the global stability of the Nudged Elastic Band with the local precision of Min-Mode Following. By introducing a stability latch, relative force triggering, and an alignment-based back-off mechanism, the method solves the instability issues that typically plague static hybrid approaches on complex potential energy surfaces.

The nudged elastic band relies on the initial path, which we assume may be reasonably obtained from an S-IDPP estimate, and that the climbing image index remains stable, with springs modulated as per the energy-weighted scheme to provide better resolution of the climbing image. We tackle the wall-time efficiency, running a local minimum mode following method to reduce the number of calls taken to converge the climbing image by a large amount. This runtime efficiency also enables converging runs with fewer images in the band.

Benchmarking against the standard Baker-Chan transition state set using a modern machine-learned potential, PET-MAD v1.1 demonstrates the practical utility of this approach. Empirically, RONEB achieves a reduction of 44% in computational cost compared to CINEB. More importantly, the method exhibits superior performance even where the standard nudged elastic band struggles due to artificial path lengthening from global rotations.

Beyond this, models accounting for the relative distance from the initial saddle to the final saddle configuration with permutation corrected distances suggests an expected improvement of 46.3% [95% CrI: -54.7%, -36.9%].

The method proves equally effective for surface systems. Tests on the OptBench Pt(111) heptamer island dataset—comprising 59 distinct diffusion mechanisms—confirm that RONEB maintains its efficiency advantage. Despite tight convergence criteria and the presence of low-frequency modes typical of surface diffusion, the hybrid protocol yielded a 28% reduction in force calls without sacrificing accuracy.

These results suggest that RONEB serves as a highly effective tool for high-throughput transition state searches, even in the context of machine-learned potentials where surface topology may deviate from the smooth harmonic basins assumed by traditional optimizers. By dynamically decoupling the saddle point search from the reaction path constraints, RONEB provides a reliable pathway to automated chemical discovery in complex systems. As machine-learned potentials reduce the cost of individual force evaluations, the computational bottleneck shifts toward optimization efficiency on rough landscapes. Additionally, the method degrades gracefully to match CINEB results, by tuning a single parameter, namely the relative change from initial path before activation of the MMF method, which holds promise for high-throughput calculations.

## 6 Conflict of Interest Statement

The authors declare that the research was conducted in the absence of any commercial or financial relationships that could be construed as a potential conflict of interest.

## 7 Author Contributions

All authors listed have made a substantial, direct and intellectual contribution to the work, and approved it for publication.

## 8 Funding

R.G. thanks the EPFL open access publishing team for institutional funding support. This research did not receive any specific grant from funding agencies in the public, commercial, or not-for-profit sectors.

## 9 Acknowledgments

R.G. acknowledges support from his family, particularly Ruhila Goswami, Prof. D. Goswami, S. Goswami, A. Goswami, and M. Sallermann. R.G. also acknowledges support from Lab-COSMO at EPFL, in particular Prof. Ceriotti and Dr. Fraux. M. G. acknowledges the support of Croatian Science Foundation, under the project HRZZ-MOBODL-2023-12-6245.

## 10 Supplemental Data

The accompanying SI contains full model specifications for the performance model, along with complete sets of visualizations for each of the 24 systems studied.

## 11 Data Availability Statement

To regenerate results, a GitHub repository contains reproduction details at [HaoZeke/nebmmf\\_repro](https://github.com/HaoZeke/nebmmf_repro), and for the analysis of data generated for this repository, a materials cloud archive [34] repository contains full trajectories including log-files and plotted results.

# Appendices

### Code for reproduction on Github. Data on Materials Archive

**Github** [https://github.com/HaoZeke/nebmmf\\_repro](https://github.com/HaoZeke/nebmmf_repro)

**Materials Archive** <https://dx.doi.org/10.24435/materialscloud:fw-wq>

## A Reproduction note

The full set of benchmark inputs, raw outputs, analysis scripts, and pinned runtime environments used in this study are publicly archived. The GitHub repository and Materials Cloud archive contain the original runs for all systems, the scripts used to generate every figure and table, and environment specifications (container/environment manifests) that reproduce the computational environment.

For the ablation study on the parameters, and for the surface systems, we ran two sets of case studies, and these logs are also provided in the archive. Users wishing to reproduce any specific experiment can either use the provided raw outputs, the pre-processed FAIR formatted csv data, or re-run the workflow using the included environment manifests and Snakemake pipelines; exact instructions and file paths are given in the archive and on the GitHub repository.

## B Computational Workflow and Hardware Utilization

To ensure reproducibility and facilitate high-throughput benchmarking across the Baker test set, we orchestrated the entire simulation pipeline using the Snakemake workflow management system [27]. This automated Directed Acyclic Graph (DAG) managed dependencies between data retrieval, endpoint relaxation, initial path generation, and the final chain-of-states optimizations.

### B.1 Environment and Software Stack

We maintained the computational environment using the pixi package manager to strictly version-control the software stack. The core simulation engine, EON<sup>5</sup>, interfaced with the PET-MAD v1.1.0 machine learning potential via the Metatomic/Metatensor library [3]. This integration allowed the C++ client to query the Python-based PyTorch model directly within the EON address space, minimizing inter-process communication overhead.

<sup>5</sup><https://eondocs.org>

## B.2 GPU Acceleration and Parallelization Strategy

We executed the benchmarks on a Lenovo ThinkStation P620 workstation equipped with an AMD Ryzen Threadripper PRO 5945WX (24 cores, 48 threads) and an NVIDIA T400 GPU (4GB VRAM). To maximize computational throughput, the Snakemake profile utilized 12 concurrent workers (`-c12`), effectively saturating the physical cores of the CPU. However, instantiating 12 independent PyTorch/CUDA contexts for the PET-MAD model would exceed the 4GB memory capacity of the T400 GPU, and provide threshing due to having to switch context several times. To resolve this, we employed the NVIDIA Multi-Process Service (MPS).

MPS acts as a bridge between the operating system and the GPU, allowing multiple processes to share a single CUDA context. By enabling the MPS control daemon (`nvidia-cuda-mps-control -d`), the 12 concurrent EON client processes submitted compute kernels to the GPU without incurring the memory overhead of individual context creation. This configuration allowed efficient, oversubscribed execution of the benchmarks on a single, entry-level workstation card.

## B.3 Performance Statistics

The raw performance data compares the standard Climbing Image Nudged Elastic Band (CINEB) against the Reorienting Off-path NEB (RONEB).

### B.3.1 Summary Statistics

- **CINEB:** Required a mean of **790.7** gradient evaluations (median: **482**) across the 24 systems.
- **RONEB:** Required a mean of **445.9** gradient evaluations (median: **230.5**).
- **Accuracy:** Both methods converged to transition states with a mean and median RMSD of 0.0 Å relative to the benchmark, with a maximum deviation of 0.3 Å, indicating they located identical saddle points.

### B.3.2 Distributional Analysis

Figure 6 presents the aggregate performance. Panel A (Cactus plot) shows the cumulative number of problems solved as a function of time (log scale), where RONEB (blue) maintains a strict advantage over CINEB (red). Panel B (Violin plot) visualizes the distribution of gradient evaluations, highlighting the reduction in the density of high-cost outliers for RONEB.

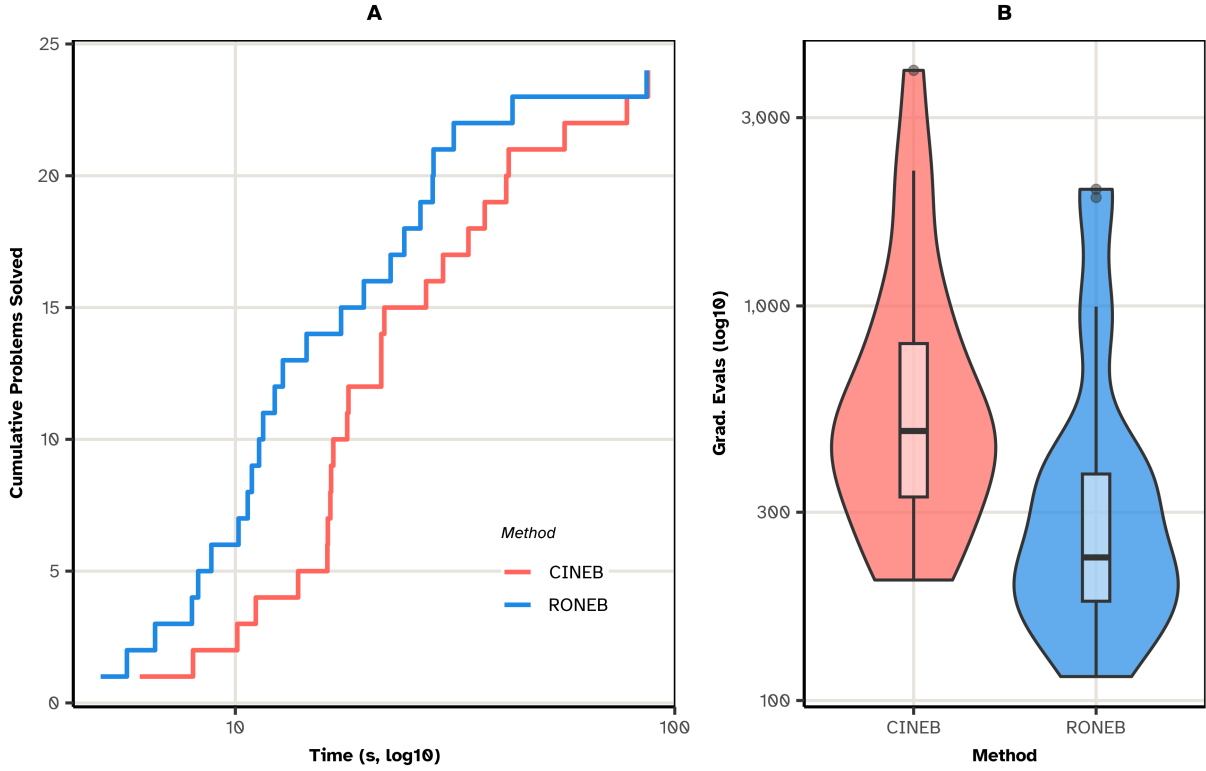


Figure 6: **Performance Distributions.** (A) Cumulative problems solved over wall-time. (B) Distribution of gradient evaluations (log scale) for CINEB and RONEB.

#### B.4 Bayesian Performance Modeling

To quantify the algorithmic efficiency while accounting for system difficulty, a Bayesian Negative Binomial regression model quantified the performance.

##### B.4.1 Model Specification

The model predicts the number of potential energy surface (PES) calls ( $y$ ) based on the method used and the quality of the initial path guess ( $x = \text{RMSD}_{\text{init}-\text{final}}$ ):

$$y_i \sim \text{NegBinomial}(\mu_i, \phi_i) \quad (13)$$

The linear predictor for the mean  $\mu$  utilizes a spline to account for the non-linear increase in cost as the initial guess degrades, grouped by the method:

$$\log(\mu_i) = \alpha + \beta_{\text{method}} + f(x)_{\text{method}} + (1|\text{System}) \quad (14)$$

The shape parameter  $\phi$ , controlling overdispersion, also varies by method:

$$\log(\phi_i) = \gamma_{\text{method}} \quad (15)$$

Priors were set as follows:

- $\beta \sim \text{Normal}(0, 1)$
- Spline SDs  $\sim \text{Exponential}(2)$

- Intercept  $\sim$  Student-t(3, 0, 2.5)
- Dispersion  $\phi \sim$  Normal(0, 0.5)

```

Family: negbinomial
Links: mu = log; shape = log
Formula: pes_calls ~ Method + s(RMSD_Init_Final, by = Method, k = 3) + (1 | System)
          shape ~ Method
Data: df_long (Number of observations: 48)
Draws: 8 chains, each with iter = 5000; warmup = 2000; thin = 1;
       total post-warmup draws = 24000

```

Smoothing Spline Hyperparameters:

	Estimate	Est.Error	1-95%		
sds(sRMSD_Init_FinalMethodCINEB_1)	0.67	0.61	0.02	2.22	1.00
sds(sRMSD_Init_FinalMethodRONEB_1)	0.63	0.58	0.02	2.13	1.00
		Bulk_ESS	Tail_ESS		
sds(sRMSD_Init_FinalMethodCINEB_1)	10827	11028			
sds(sRMSD_Init_FinalMethodRONEB_1)	12279	11499			

Multilevel Hyperparameters:

	Estimate	Est.Error	1-95%		
~System (Number of levels: 24)					
sd(Intercept)	0.43	0.09	0.28	0.62	1.00
				4800	8431

Regression Coefficients:

	Estimate	Est.Error	1-95%		
Intercept	6.38	0.11	6.16	6.59	1.00
shape_Intercept	2.60	0.41	1.80	3.42	1.00
MethodRONEB	-0.62	0.08	-0.79	-0.46	1.00
shape_MethodRONEB	0.12	0.46	-0.81	1.03	1.00
sRMSD_Init_Final:MethodCINEB_1	0.54	0.11	0.32	0.76	1.00
sRMSD_Init_Final:MethodRONEB_1	0.55	0.10	0.34	0.76	1.00
		Tail_ESS			
Intercept		10286			
shape_Intercept		12216			
MethodRONEB		16755			
shape_MethodRONEB		15483			
sRMSD_Init_Final:MethodCINEB_1		8380			
sRMSD_Init_Final:MethodRONEB_1		7688			

Draws were sampled using `sample(hmc)`. For each parameter, Bulk\_ESS and Tail\_ESS are effective sample size measures, and Rhat is the potential scale reduction factor on split chains (at convergence, Rhat = 1).

With the exact results in Table 6.

Table 6: Results of the PES model

Effect_Type	Median Effect	95% CrI
Expected PES Calls (Baseline: CINEB)	587.4	[473.9, 725.7]
Multiplicative Factor (RONEB vs CINEB)	0.5	[0.45, 0.63]
Percentage Change (RONEB vs CINEB)	-46.3%	[-54.7%, -36.9%]

Essentially, the model estimates the following effects:

**Baseline Expectation** The expected number of gradient calls for the baseline CINEB method is 587.4 [95% CrI: 473.9, 725.7].

**RONEB Efficiency** The multiplicative factor for RONEB relative to CINEB is 0.5 [95% CrI: 0.45, 0.63].

**Reduction** This corresponds to a percentage change of **-46.3%** [95% CrI: -54.7%, -36.9%] in computational effort.

#### B.4.2 Posterior Results

The model estimates the following effects:

- **Baseline Expectation:** The expected number of gradient calls for the baseline CINEB method is 587.4 [95% CrI: 473.9, 725.7].
- **RONEB Efficiency:** The multiplicative factor for RONEB relative to CINEB is 0.5 [95% CrI: 0.45, 0.63].
- **Reduction:** This corresponds to a percentage change of **-46.3%** [95% CrI: -54.7%, -36.9%] in computational effort.

#### B.4.3 Shape Parameter Analysis

The shape parameter  $\phi$  of the Negative Binomial distribution controls overdispersion (higher values indicate more consistency/less variance). Figure 7 illustrates the posterior density of the shape parameter for both algorithms.

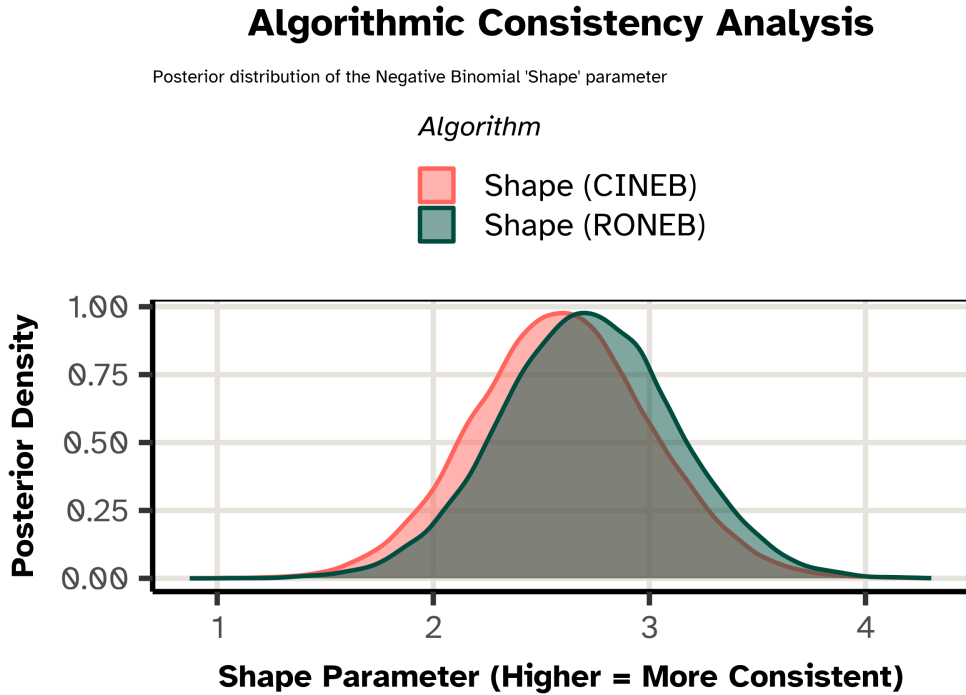


Figure 7: **Algorithmic Consistency.** Posterior distribution of the Negative Binomial shape parameter. RONEB exhibits a similar dispersion profile to CINEB, indicating that the speedup does not come at the cost of erratic variance.

#### B.4.4 Input Domain Validity

To ensure the spline term  $f(x)$  was valid, we verified the distribution of the independent variable (RMSD between initial and final saddle). Figure 8 confirms data density across the linear range of 0.1 Å to 0.8 Å.

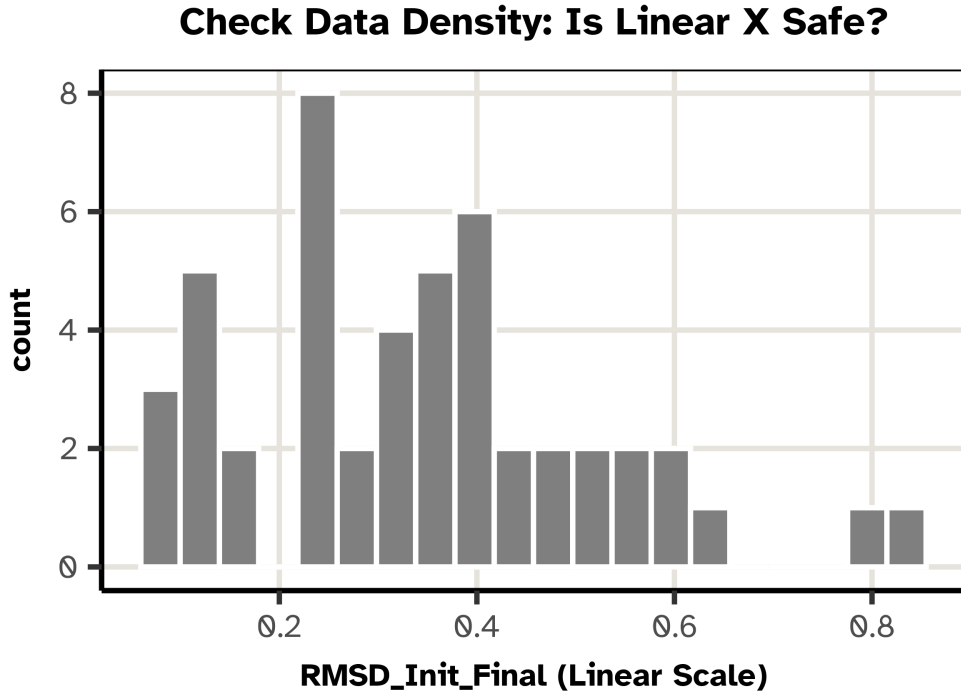


Figure 8: **Input Density.** Histogram of  $\text{RMSD}_{\text{Init}} \backslash \text{Final}$  values, confirming sufficient data density to support the spline term in the regression model.

## B.5 Model Diagnostics

We performed extensive posterior predictive checks (PPC) and Leave-One-Out (LOO) cross-validation to validate the model fit.

### B.5.1 Posterior Predictive Density

Figure 9 compares the observed distribution of gradient calls ( $y$ , dark line) with 50 distributions simulated from the posterior ( $y_{rep}$ , light lines). The model accurately reproduces the heavy tail of the cost distribution.

## Posterior Predictive Check: Density

Does the model reproduce the distribution of gradient calls?

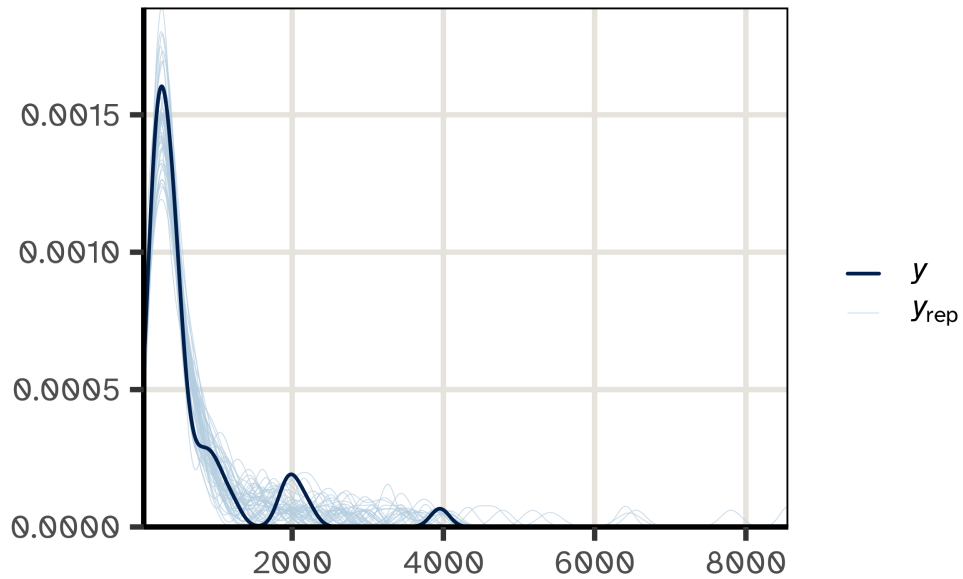


Figure 9: **Posterior predictive density check.** The model successfully captures the data generating process for gradient evaluations.

### B.5.2 Grouped Intervals

Figure 10 verifies that the model fits both experimental groups (CINEB and RONEB) equally well, with observed data points falling within the predicted credible intervals.

## Posterior Predictive Check: Intervals by Method

Do the observed data points (dots) fall within the predicted ranges (bars)?

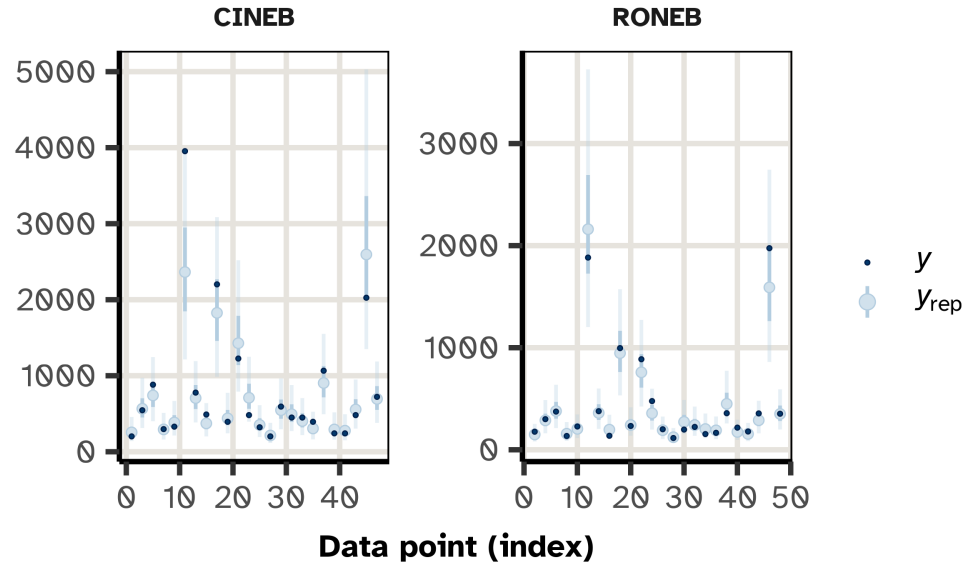


Figure 10: Posterior predictive intervals grouped by Method.

### B.5.3 LOO-PIT and Pareto-k

The Probability Integral Transform (PIT) check (Figure 11) shows that the resulting distribution is uniform, indicating well-calibrated error estimates. Furthermore, all Pareto  $k$  estimates from the LOO cross-validation remained below 0.7, confirming the reliability of the importance sampling.

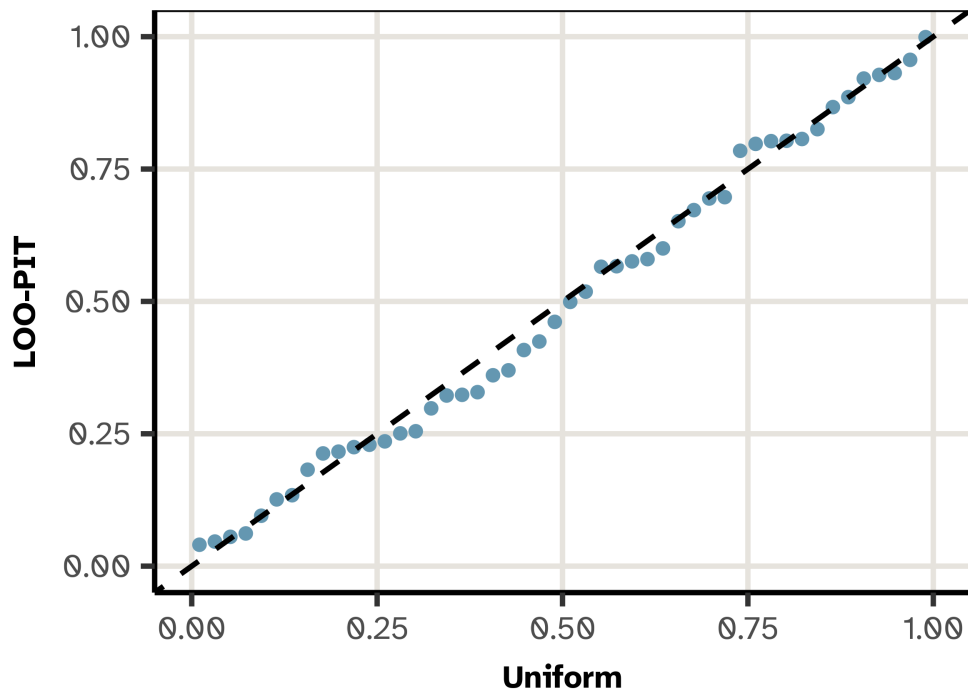


Figure 11: **LOO-PIT Q-Q plot against a uniform distribution.** The alignment with the diagonal indicates the model is well-calibrated.

## References

- [1] ÁSGEIRSSON, V., BIRGISSON, B. O., BJORNSSON, R., BECKER, U., NEESE, F., RIPLINGER, C., AND JÓNSSON, H. Nudged Elastic Band Method for Molecular Reactions Using Energy-Weighted Springs Combined with Eigenvector Following. *Journal of Chemical Theory and Computation* 17, 8 (Aug. 2021), 4929–4945.
- [2] BAKER, J., AND CHAN, F. The location of transition states: A comparison of Cartesian, Z-matrix, and natural internal coordinates. *Journal of Computational Chemistry* 17, 7 (1996), 888–904.
- [3] BIGI, F., ABBOTT, J. W., LOCHE, P., MAZITOV, A., TISI, D., LANGER, M. F., GOSCINSKI, A., PEGOLO, P., CHONG, S., GOSWAMI, R., CHORNA, S., KELLNER, M., CERIOTTI, M., AND FRAUX, G. Metatensor and metatomic: Foundational libraries for interoperable atomistic machine learning, Aug. 2025.
- [4] CERJAN, C. J., AND MILLER, W. H. On finding transition states. *The Journal of Chemical Physics* 75, 6 (Sept. 1981), 2800–2806.
- [5] CHAPRA, S. C., AND CANALE, R. P. *Numerical Methods for Engineers*, 7. ed ed. McGraw-Hill Education, New York, NY, 2015.
- [6] CHILL, S. T., STEVENSON, J., RUEHLE, V., SHANG, C., XIAO, P., FARRELL, J. D., WALES, D. J., AND HENKELMAN, G. Benchmarks for Characterization of Minima, Transition States, and Pathways in Atomic, Molecular, and Condensed Matter Systems. *Journal of Chemical Theory and Computation* 10, 12 (Dec. 2014), 5476–5482.
- [7] GOSWAMI, R. Bayesian hierarchical models for quantitative estimates for performance metrics applied to saddle search algorithms. *AIP Advances* 15, 8 (Aug. 2025), 85210.
- [8] GOSWAMI, R. Efficient exploration of chemical kinetics, Oct. 2025.
- [9] GOSWAMI, R. Two-dimensional RMSD projections for reaction path visualization and validation, Dec. 2025.
- [10] GOSWAMI, R., AND JÓNSSON, H. Adaptive Pruning for Increased Robustness and Reduced Computational Overhead in Gaussian Process Accelerated Saddle Point Searches. *ChemPhysChem* (Nov. 2025).
- [11] GOSWAMI, R., MASTEROV, M., KAMATH, S., PEÑA-TORRES, A., AND JÓNSSON, H. Efficient implementation of gaussian process regression accelerated saddle point searches with application to molecular reactions, May 2025.
- [12] GOSWAMI, R., MASTEROV, M., KAMATH, S., PEÑA-TORRES, A., AND JÓNSSON, H. Efficient Implementation of Gaussian Process Regression Accelerated Saddle Point Searches with Application to Molecular Reactions. *Journal of Chemical Theory and Computation* (July 2025).
- [13] GUNDE, M., SALLES, N., GRISANTI, L., MARTIN-SAMOS, L., AND HEMERYCK, A. SOFI: Finding point group symmetries in atomic clusters as finding the set of degenerate solutions in a shape-matching problem. *The Journal of Chemical Physics* 161, 6 (Aug. 2024), 062503.
- [14] GUNDE, M., SALLES, N., HÉMERYCK, A., AND MARTIN-SAMOS, L. IRA: A shape matching approach for recognition and comparison of generic atomic patterns. *Journal of Chemical Information and Modeling* 61, 11 (Nov. 2021), 5446–5457.
- [15] HENKELMAN, G., AND JÓNSSON, H. A dimer method for finding saddle points on high dimensional potential surfaces using only first derivatives. *The Journal of Chemical Physics* 111, 15 (Oct. 1999), 7010–7022.
- [16] HENKELMAN, G., AND JÓNSSON, H. Improved tangent estimate in the nudged elastic band method for finding minimum energy paths and saddle points. *The Journal of Chemical Physics* 113, 22 (Dec. 2000), 9978–9985.
- [17] HENKELMAN, G., UBERUAGA, B. P., AND JÓNSSON, H. A climbing image nudged elastic band method for finding saddle points and minimum energy paths. *The Journal of Chemical Physics* 113, 22 (Nov. 2000), 9901–9904.
- [18] HEYDEN, A., BELL, A. T., AND KEIL, F. J. Efficient methods for finding transition states in chemical reactions: Comparison of improved dimer method and partitioned rational function optimization method. *The Journal of Chemical Physics* 123, 22 (Dec. 2005), 224101.
- [19] JONSSON, H., MILLS, G., AND JACOBSEN, K. W. Nudged elastic band method for finding minimum energy paths of transitions. In *Classical and Quantum Dynamics in Condensed Phase Simulations*. World Scientific, June 1998, pp. 385–404.
- [20] KÄSTNER, J., AND SHERWOOD, P. Superlinearly converging dimer method for transition state search. *The Journal of Chemical Physics* 128, 1 (Jan. 2008), 014106.

[21] KOISTINEN, O.-P., ÁSGEIRSSON, V., VEHTARI, A., AND JÓNSSON, H. Nudged Elastic Band Calculations Accelerated with Gaussian Process Regression Based on Inverse Interatomic Distances. *Journal of Chemical Theory and Computation* 15, 12 (Dec. 2019), 6738–6751.

[22] KOISTINEN, O.-P., ÁSGEIRSSON, V., VEHTARI, A., AND JÓNSSON, H. Minimum Mode Saddle Point Searches Using Gaussian Process Regression with Inverse-Distance Covariance Function. *Journal of Chemical Theory and Computation* 16, 1 (Jan. 2020), 499–509.

[23] LIU, D. C., AND NOCEDAL, J. On the limited memory BFGS method for large scale optimization. *Mathematical Programming* 45, 1 (Aug. 1989), 503–528.

[24] MANDELLI, D., AND PARRINELLO, M. A modified nudged elastic band algorithm with adaptive spring lengths. *Journal of Chemical Physics* 155, 7 (Aug. 2021), 74103.

[25] MAZITOV, A., BIGI, F., KELLNER, M., PEGOLO, P., TISI, D., FRAUX, G., POZDNYAKOV, S., LOCHE, P., AND CERIOTTI, M. PET-MAD as a lightweight universal interatomic potential for advanced materials modeling. *Nature Communications* 16, 1 (Nov. 2025), 10653.

[26] MAZITOV, A., CHORNA, S., FRAUX, G., BERCX, M., PIZZI, G., DE, S., AND CERIOTTI, M. Massive atomic diversity: A compact universal dataset for atomistic machine learning. *Scientific Data* 12, 1 (Nov. 2025), 1857.

[27] MÖLDER, F., JABLONSKI, K. P., LETCHER, B., HALL, M. B., TOMKINS-TINCH, C. H., SOCHAT, V., FORSTER, J., LEE, S., TWARDZIOK, S. O., KANITZ, A., WILM, A., HOLTGREWE, M., RAHMANN, S., NAHNSEN, S., AND KÖSTER, J. Sustainable data analysis with Snakemake, Apr. 2021.

[28] MUNRO, L. J., AND WALES, D. J. Defect migration in crystalline silicon. *Physical Review B* 59, 6 (Feb. 1999), 3969–3980.

[29] OLSEN, R. A., KROES, G. J., HENKELMAN, G., ARNALDSSON, A., AND JÓNSSON, H. Comparison of methods for finding saddle points without knowledge of the final states. *The Journal of Chemical Physics* 121, 20 (Nov. 2004), 9776–9792.

[30] PARK, H., PRITCHARD, B. P., AND WANG, L.-P. High-throughput approach for minimum energy pathway search using the nudged elastic band method with efficient data handling and parallel computing. *Journal of Chemical Theory and Computation* 21, 23 (Dec. 2025), 12048–12063.

[31] PETERSON, A. A. Acceleration of saddle-point searches with machine learning. *The Journal of Chemical Physics* 145, 7 (Aug. 2016), 074106.

[32] SCHMERWITZ, Y. L. A., ÁSGEIRSSON, V., AND JÓNSSON, H. Improved Initialization of Optimal Path Calculations Using Sequential Traversal over the Image-Dependent Pair Potential Surface. *Journal of Chemical Theory and Computation* 20, 1 (Jan. 2024), 155–163.

[33] SMIDSTRUP, S., PEDERSEN, A., STOKBRO, K., AND JÓNSSON, H. Improved initial guess for minimum energy path calculations. *The Journal of Chemical Physics* 140, 21 (June 2014), 214106.

[34] TALIRZ, L., KUMBHAR, S., PASSARO, E., YAKUTOVICH, A. V., GRANATA, V., GARGIULO, F., BORELLI, M., UHRIN, M., HUBER, S. P., ZOUPANOS, S., ADORF, C. S., ANDERSEN, C. W., SCHÜTT, O., PIGNEDOLI, C. A., PASSERONE, D., VANDEVONDELE, J., SCHULTHESS, T. C., SMIT, B., PIZZI, G., AND MARZARI, N. Materials cloud, a platform for open computational science. *Scientific Data* 7, 1 (Sept. 2020), 299.